npj | advanced manufacturing

Article

https://doi.org/10.1038/s44334-025-00016-1

Distance-controlled direct ink writing of titanium alloy with enhanced shape diversity and controllable porosity

Erick Bandala[1,7], Lily Raymond[1,7], Kellen Mitchell[1,7], Fazlay Rubbi[2], John Thella[3], Bankole O. Osho[3], Amanendra K. Kushwaha[1], Mohammadreza Elahifard[4], Ji Su[5], Xing Zhang[6], Pradeep L. Menezes[1] ✉, Xiaoliang Wang[4] ✉, Pengbo Chu[3] ✉, Yiliang Liao[2] ✉ & Yifei Jin[1] ✉

Porous titanium alloys have been extensively used for diverse engineering applications. However, current additive manufacturing (AM) strategies face significant challenges (e.g., low fabrication efficiency and limited shape diversity) in producing porous titanium alloys. This work aims to develop a distance-controlled direct ink writing (DC-DIW) approach for constructing macroscale 3D architectures from titanium alloy powders. This approach integrates a constant interlayer distance control with traditional DIW, breaking through the angle limit in current porous metal printing from 60° to 30°. Additionally, subsequent heat treatment is applied to control microstructures. To demonstrate the capabilities of this approach, three representative structures, including a bifurcated tube, an orbital implant, and a knee implant, are successfully printed and treated, achieving suitable mechanical properties and high shape fidelity. This work provides a viable and efficient AM strategy for fabricating porous titanium alloys with enhanced shape diversity and controllable porosity suitable for various engineering applications.

Porous metals are materials characterized by high and controllable porosity, with microscale pores that are either interconnected or isolated[1–3]. Common materials used to make porous metals include aluminum, titanium, copper, nickel, and their alloys[4–7]. Among these, titanium alloys are significant because of their unique properties, such as high strength-to-weight ratio[8], excellent corrosion resistance[9], and good biocompatibility[10]. Particularly, porous titanium alloys offer high toughness and low stiffness, which help avoid stress-shielding[11] and enhance biocompatibility and osseointegration[12–14]. Additionally, porous titanium alloys provide customizable mechanical properties[15,16], making them extensively used in various engineering applications[17–19].

In contrast to traditional manufacturing methods (e.g., powder metallurgy[20] and forming techniques[21]), additive manufacturing (AM) is an emerging technology that allows for the creation of metal products with customized designs and complex architectures[22]. There are two main strategies for the fabrication of porous metals using AM: (1) pixel-by-pixel based and (2) sacrificial additive based. In the first strategy, a high-energy laser or electron beam spot is used to selectively sinter and/or melt metal powders in a pixel-by-pixel manner to create each pore and the overall architecture. Representative AM methods for this strategy include selective laser sintering[23], electron beam melting[24], and direct metal laser sintering[25]. While this approach can produce pores with complex internal structures and accurately control porosity, its pixel-by-pixel printing method significantly reduces fabrication efficiency, especially for scaling up porous metallic products[26–28]. In addition, the high cost of the equipment needed for generating high-energy lasers and electron beams increases the manufacturing cost.

To improve fabrication efficiency and reduce manufacturing costs, recent advancements have focused on the sacrificial additive-based strategy. In this strategy, metal powders are mixed with sacrificial additives/particles and solvents to prepare build materials. Generally, direct ink writing (DIW), a cost-effective material extrusion three-dimensional (3D) printing technique, is used to extrude the build material through a nozzle, forming continuous filaments that are deposited layer-by-layer to create a predefined macroscale structure. Subsequently, heat treatment is performed to burn out the sacrificial additives and solvents, resulting in microscale pores.

[1]Department of Mechanical Engineering, University of Nevada Reno, Reno, NV, USA. [2]Department of Industrial and Manufacturing Systems Engineering, Iowa State University, Ames, IA, USA. [3]Department of Mining and Metallurgical Engineering, University of Nevada Reno, Reno, NV, USA. [4]Division of Atmospheric Sciences, Desert Research Institute, Reno, NV, USA. [5]Advanced Materials and Processing Branch, NASA Langley Research Center, Hampton, VA, USA. [6]School of Mechanical and Electrical Engineering, Soochow University, Suzhou, China. [7]These authors contributed equally: Erick Bandala, Lily Raymond, Kellen Mitchell. ✉e-mail: pmenezes@unr.edu; xiaoliang.wang@dri.edu; pengboc@unr.edu; leonl@iastate.edu; yifeij@unr.edu

This strategy has been adopted to print various porous metals and alloys. For instance, Chen et al.[29] fabricated microlattices from high-entropy superalloys using a three-step process: printing 3D structures with the ink composed of elemental powders and titanium alloy powders, sintering to densify and homogenize the structures, and aging to tune the microstructure. Valentin et al.[30] developed a self-supporting titanium-6% aluminum-4% vanadium (Ti64) ink consisting of Ti64 powders and a polymer/particle matrix to print 3D structures which were further sintered in a furnace to produce Ti64 parts. Xu et al.[31] combined DIW with vacuum sublimation to manufacture porous implants, using DIW for constructing macroscale structures and sublimation of manganese to create micropores in the structures. However, due to the poor interlayer bonding strength, DIW is limited to creating simple geometries such as lattices[29], 60°-tubes, honeycombs[30], and scaffolds[30,31]. For more complex designs with overhanging sections at angles below 60°, numerous supporting scaffolds are required, similar to the structure limitation in fused deposition modeling (FDM)[32]. For example, Xu et al.[33] developed a multi-material DIW method to fabricate complex 3D steel architectures with supporting scaffolds made from sacrificial, low melting-point metals like copper. Despite these advancements, some challenges still remain, including additional post-treatments to remove scaffolds and high material waste. Therefore, it is necessary to improve DIW approaches to produce porous metals with enhanced shape diversity and minimized material waste.

In this work, a distance-controlled direct ink writing (DC-DIW) approach is introduced. This approach integrates a constant interlayer distance control method with traditional DIW to construct macroscale 3D architectures from a slurry ink composed of titanium alloy powders and sacrificial additives embedded in a polymer matrix. After printing, heat treatment is applied to remove the sacrificial components, sinter titanium alloy powders, and control the resulting pore geometries at the microscale. The DC-DIW approach aims to overcome the angle limit of traditional DIW, extending it from 60° to 30°. This innovative method offers a viable and efficient AM strategy for fabricating porous titanium alloys with enhanced shape diversity and controllable porosity for a wide range of engineering applications.

Results

Mechanism of the DC-DIW approach

The schematic of the proposed DC-DIW approach is illustrated in Fig. 1. In the material preparation step, the Ti64 slurry ink comprises four key components as follows. (1) Ti64 powders are employed as the metallic component to create functional products after sintering. (2) Bentonite particles act as the yield-stress additive. Bentonite is a type of nanoclay with negatively charged faces and positively charged edges, enabling the electrostatic interactions between particles. When dispersed in a solvent, bentonite particles form a unique "house-of-cards" arrangement, which provides a self-supporting capability for DIW and stabilizes Ti64 powders to prevent undesired particle aggregation[34–36]. Since the ink is self-supporting, crosslinking between layers is unnecessary and not preferred, as it may cause interfacial stress and/or incomplete fusion between newly deposited liquid layers and previous crosslinked layers, negatively affecting the integrity and mechanical properties of as-printed parts[37]. (3) Polyethylene glycol diacrylate (PEGDA) is used as the polymer solvent to support the printed structure after UV crosslinking. (4) The photoinitiator (PI) drives the crosslinking of PEGDA under UV radiation. These components are shown in Fig. 1A.

In the DIW step, the Ti64 slurry ink is loaded into a syringe. Because the external shear stress is lower than the ink's yield stress, the "house-of-cards" arrangement remains intact. At the macroscale, the Ti64 slurry ink presents in a solid state (inset of Fig. 1B1). When high-pressure air is applied, the ink is extruded through a dispensing nozzle. Within the nozzle, the external shear stress increases and exceeds the ink's yield stress, disrupting the "house-of-cards" arrangement (inset of Fig. 1B2). This disruption induces the ink to transition from a solid-like state to a liquid state at the macroscale. After deposition, the external shear stress significantly decreases, allowing the bentonite's "house-of-cards" arrangement to rebuild. Consequently, the ink transitions back from a liquid to a solid-like state, enabling the printed structure to stably maintain its as-printed architecture even without crosslinking.

Following printing, a photocrosslinking step is performed by exposing the 3D structure to UV radiation, as shown in Fig. 1C. The photoinitiator (Irgacure 2959 in this work) absorbs UV photons, leading to homolytic cleavage of molecules and the generation of free radicals[38–40]. These radicals react with the carbon-carbon double bonds (C=C) in the acrylate groups of PEGDA to form new radicals that react with acrylate groups on other PEGDA molecules, creating covalent bonds and forming a 3D network within the printed structure (inset of Fig. 1C)[41,42]. This network provides permanent and robust support, stabilizing the architecture[43].

Finally, a multi-step heat treatment is conducted in a vacuum furnace. During the first and second steps, PEGDA and bentonite are removed from the structure at 500[30,44] and 800 °C[30,45], respectively. In the third step, the temperature is increased to promote solid-state sintering of Ti64 powders, as

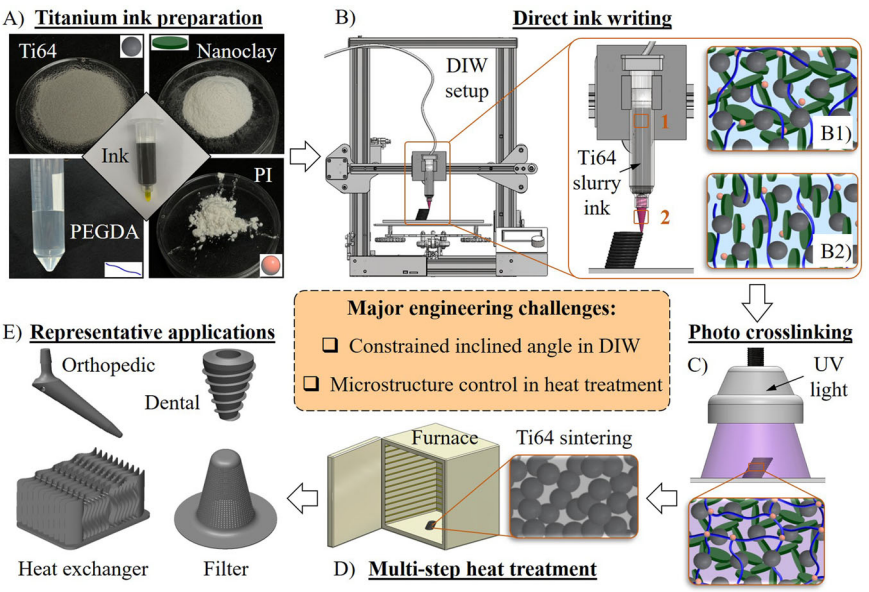

Fig. 1 | Schematic of the proposed DC-DIW approach. A Preparation of the Ti64 slurry ink. **B** DIW of the Ti64 slurry ink into a pre-defined 3D structure and the microstructure evolution **B1** without and **B2** with external shear stress. **C** Photocrosslinking to induce the solidification of the printed structure. **D** Multi-step heat treatment to remove unnecessary components and sinter Ti64 powders. **E** Representative applications of the printed porous metal structure.

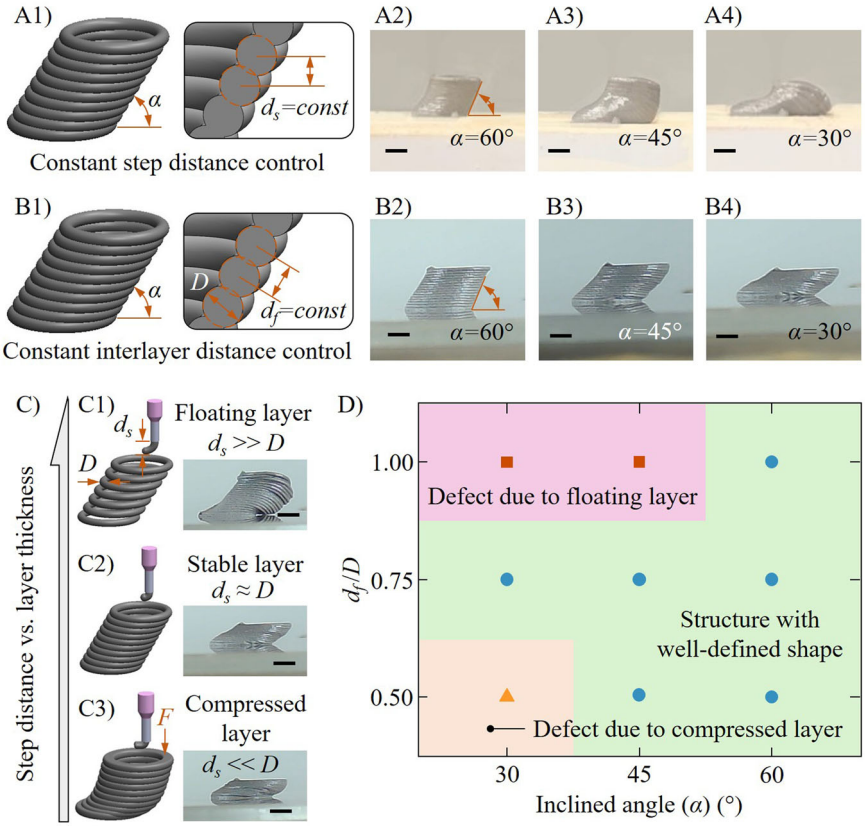

Fig. 2 | Effects of key printing parameters on shape diversity. A Constant step distance control method in current DIW: **A1** schematic and printed tubes with the inclined angle of **A2** 60°, **A3** 45°, and **A4** 30°. **B** The proposed constant interlayer distance control method in DC-DIW: **B1** schematic and printed tubes with the inclined angle of **B2** 60°, **B3** 45°, and **B4** 30°. **C** Effects of interlayer distance: formation of **C1** floating layer, **C2** stable layer, and **C3** compressed layer at different conditions. **D** Phase diagram to summarize the effects of two dimensionless numbers on the shape diversity. Scale bars: 5 mm.

shown in Fig. 1D. The pore characteristics, such as pore size and porosity, are influenced by the sintering temperature and duration. The resulting porous metal structure features a well-defined macroscale architecture and a controllable microstructure, making it suitable for diverse engineering applications, including orthopedic and dental implants, filters, and heat exchangers (Fig. 1E). This work aims to address two major engineering challenges in current methods for constructing porous metals: the constrained inclined angle (>60°) in the DIW step and microstructure control during heat treatment.

Effects of key printing parameters on shape diversity

In traditional DIW, a constant step distance (d_s), also called layer height, is controlled between layers to print 3D structures in air, as shown in Fig. 2A1. This approach imposes significant limitations when printing overhanging architectures. For instance, as illustrated in Fig. 2A2–A4, the tube structure can maintain its overall shape when the inclined angle (φ) is 60°. However, as φ decreases to 45°, the tube structure partially collapses, and at φ of 30°, the structure completely collapses. Consequently, external scaffolds are often required for printing overhanging sections with an inclined angle of less than 60°. This is because the bonding strength between layers is influenced by the interlayer distance (d_f), instead of the step distance, which can be described by $d_f = d_s/\sin\varphi$. Thus, as φ decreases from 90° to 30°, d_f increases twofold at a constant step distance, which results in a reduced contact area between layers. Therefore, the previously deposited layers cannot adequately support subsequent ones, leading to the collapse of the printed tubes.

In the proposed DC-DIW approach, d_f is controlled (Fig. 2B1) to mitigate the challenges associated with varying inclined angles. As shown in Fig. 2B2–B4, three tubes with inclined angles of 60°, 45°, and 30° are printed via DC-DIW. Due to the sufficient contact area between layers, these tubes exhibit high interlayer bonding strength and overall structural stability. Specifically, even when φ is 30°, the printed tube still maintains its shape with much of the structure suspended above the substrate.

In addition to the interlayer distance, the filament diameter (D) also affects the contact area and bonding strength between layers. To illustrate the effects of these critical printing parameters (d_f and D) on the shape diversity of printable structures, a dimensionless ratio $\beta = d_f/D$ is defined. When the interlayer distance exceeds the filament diameter (e.g., $\beta \geq 1.0$), floating layers are deposited without sufficient contact area, leading to the collapse of the printed tube with each layer, as illustrated in Fig. 2C1. When $\beta \approx 0.75$, the proposed DC-DIW approach effectively prints a 30° tube with well-defined geometries (Fig. 2C2). Conversely, when d_f is much smaller than D (e.g., $\beta \leq 0.5$), the compression from the nozzle tip and extruded ink exceeds the yield stress of the Ti64 slurry ink, causing deformation (Fig. 2C3) or even the failure of the entire tube structure. By coupling β with another dimensionless ratio $\sin\varphi$, diverse tubes can be printed with varying parameters, as summarized in the phase diagram in Fig. 2D. It is observed that when β is around 0.75, the proposed DC-DIW approach can effectively print tubes with various inclined angles. In contrast, when β is outside the optimal range (e.g., less than 0.5 and/or higher than 1.0), DC-DIW can only produce overhanging sections with steeper inclined angles. This phase diagram serves as a guideline for selecting suitable printing parameters to create diverse 3D structures via DC-DIW.

Microstructure control by multi-step heat treatment

An essential requirement for porous metals is the ability to control microstructural features, such as pore size and porosity, which significantly impact the mechanical properties at the macroscale. This control also enhances other beneficial properties, including corrosion resistance in chemical engineering[46], thermal insulation in aerospace applications[18], and cell proliferation in biomedical fields[47,48]. This work investigates the effects of temperature and time, two critical sintering parameters, on porous microstructure formation and the resultant mechanical properties.

Initially, the samples made from Ti64 slurry ink are sintered in the vacuum furnace at three temperatures (1200, 1350, and 1500 °C) for 2 h. The relative densities of these samples (with the density of bulk Ti64 as the

reference) are shown in Fig. S1. As the sintering temperature increases from 1200 to 1500 °C, the relative density decreases from 92.6 ± 0.88 to 89.9 ± 0.79%. This decrease is attributed to variations in the microstructures. As illustrated in Fig. S2, both the porosity and pore size increase with the increasing sintering temperature: the porosity rises from 7.4 ± 0.88 to 10.1 ± 0.79% (Fig. S2A), and the pore size increases from 5.17 ± 0.48 to 34.41 ± 2.22 μm (Fig. S2B). The same trend is also observed for the nanoscale pores, as shown in Fig. S3. This is because the increase in temperature leads to the expansion of encapsulated gases within the printed structure (i.e., carbon monoxide and carbon dioxide), which are generated from the thermal degradation of PEGDA[44,49] and bentonite[44,45]. Additionally, the short sintering time does not allow sufficient gas expulsion to enable effective solid-state sintering of Ti64 powders[50], leading to larger pores, increased porosity, and reduced relative density. The microstructure images of the samples sintered at different temperatures (Fig. S4) reveal a decrease in the neck width among adjacent Ti64 powders from 47.84 ± 1.76 to 26.86 ± 2.60 μm, as shown in Table S1. This change is consistent with the increase in the mesoscale pore size from 5.17 ± 0.48 μm to 34.41 ± 2.22 μm.

Despite the lower relative density at 1500 °C, this temperature remains the most effective for enhancing solid-state sintering. To further investigate its effect, the sintering time is extended from 2 to 6 h. Sintering for extended durations, such as 8 or 10 h at high temperatures, may be detrimental to the samples, as excessive sintering results in significant grain growth, which may lead to strength loss[51,52]. As shown in Fig. 3A, extending the sintering time increases the relative density from 89.9 ± 0.79 to 93.3 ± 0.35% due to the enhanced sintering among Ti64 powders[53,54]. This explanation is supported by the change in porosity and pore size. As shown in Fig. 3B, the porosity decreases from 10.1 ± 0.79 to 6.7 ± 0.35%. Simultaneously, the mesoscale pore size decreases significantly from 34.41 ± 2.22 to 7.16 ± 0.56 μm, as illustrated in Fig. 3C, while the nanoscale pore size also reduces from 209.27 to 87.27 nm, as shown in Fig. S5. Therefore, the prolonged sintering leads to the shrinkage and closure of many pores, densifying the fabricated

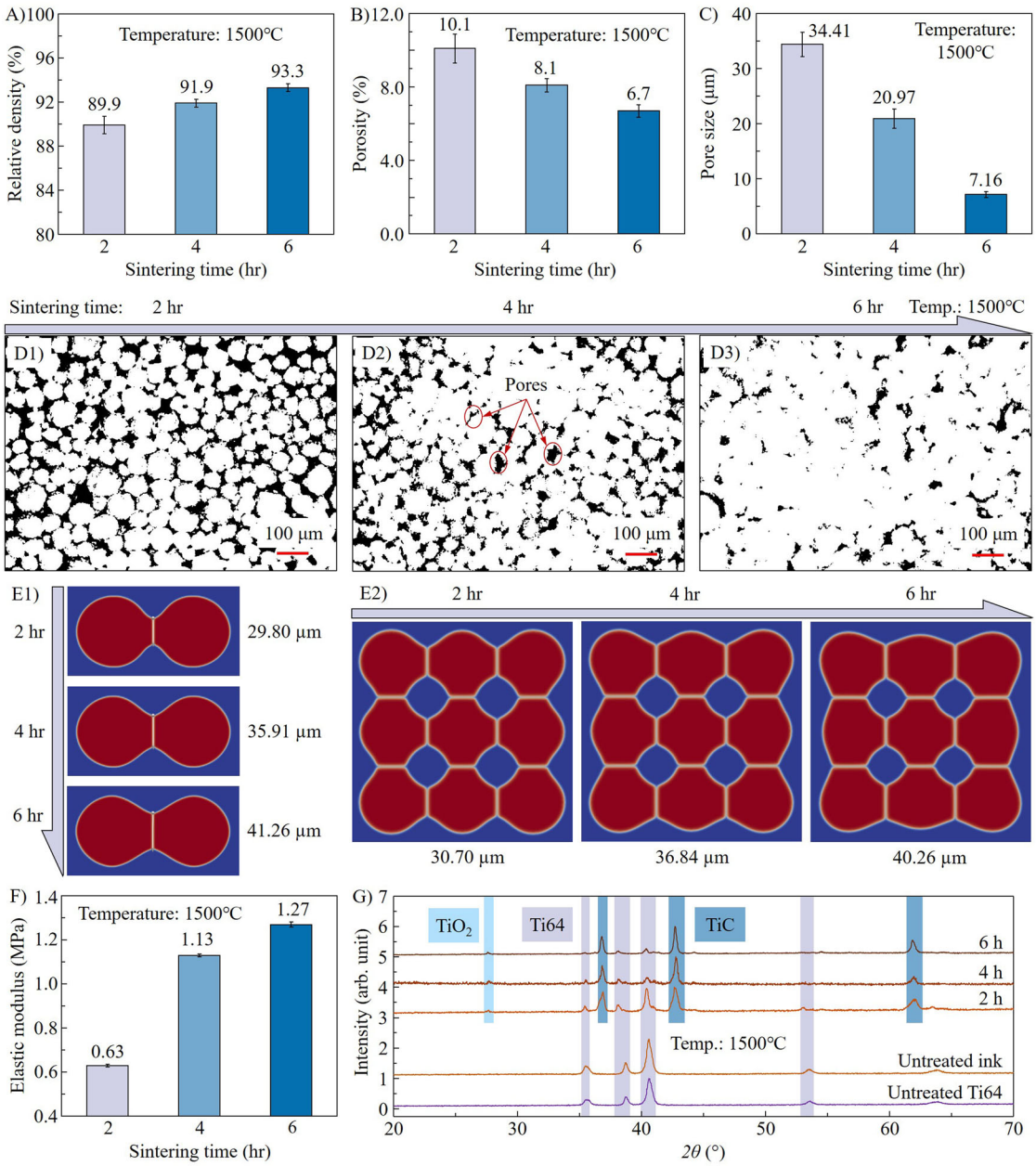

Fig. 3 | Characteristics of porous Ti64 structure after multi-step heat treatment. Effects of sintering time on **A** relative density, **B** porosity, and **C** pore size. **D** Microstructure images of the Ti64 samples sintered for different time durations at 1500 °C. **E** PF modeling results: sintering of **E1** two and **E2** multiple Ti64 powders for different time durations at 1500 °C. **F** Effects of sintering time on elastic modulus. **G** Crystal structures of the porous Ti64 samples before and after sintering.

structures[50,52]. The pore size change is also visible in the images in Fig. 3D. Based on the measurements in Table S2, the average neck width increases from 26.86 ± 2.60 to 55.63 ± 2.83 μm, indicating the ongoing solid-state sintering.

To identify the mechanisms responsible for the microstructure evolution during solid-state sintering, the phase-field (PF) modeling[55–59] is employed to simulate the sintering of Ti64 powders with a diameter of 80 μm. The details in the modeling are summarized in Supporting Information S7. The particle coalescence and neck formation at different temperatures (i.e., 1200, 1350, and 1500 °C) are illustrated in Fig. S6. It is observed that the neck width for two separated particles increases from 0 to 29.80 μm with the increasing temperature, while the neck width for nine particles also increases from 23.86 to 30.70 μm. The simulation results are not consistent with the experimental results in Table S1. This is because, at the short sintering time of 2 h, gas expansion may affect the solid-state sintering more than surface diffusion and grain boundary diffusion. In the PF modeling, this factor is not considered, leading to the deviation between the simulated and experimental results. However, when the temperature is elevated to 1500 °C, the gas generated from the thermal degradation of PEGDA and bentonite is expulsed and its effects on the microstructure evolution are negligible. In this case, the neck width of two separated particles increases gradually from 29.80 to 41.26 μm as the sintering period extends from 2 to 6 h, as shown in Fig. 3E1. A similar result is also obtained when simulating the sintering process of nine particles: the neck width increases from 30.70 to 40.26 μm (Fig. 3E2), which matches well with the experimental data as summarized in Table S2. This consistency indicates that at elevated temperatures, the surface diffusion and grain boundary diffusion dominate the sintering process and significantly affect the microstructure formation.

The evolution of the microstructure significantly impacts the mechanical properties of porous metal structures at the macroscale. Fig. S7A illustrates the stress-strain curves for the samples sintered at different temperatures, while Fig. S7B depicts their corresponding elastic moduli. The data shows that as the sintering temperature increases, the elastic modulus decreases from 0.98 ± 0.010 to 0.63 ± 0.006 MPa. This trend aligns with the observed changes in relative density, porosity, and pore size as detailed in Supporting Information S1, S2, and S3. Furthermore, the samples sintered for different durations are analyzed, with the stress-strain curves shown in Fig. S8. The elastic modulus of these samples increases from 0.63 ± 0.006 to 1.27 ± 0.012 MPa when the sintering extends from 2 to 6 h at 1500 °C, as shown in Fig. 3F. This increase suggests that prolonging the sintering time at an elevated temperature enhances the solid-state sintering of Ti64 powders, thereby improving the mechanical properties[52,60].

Detection of residues after sintering

It is worth noting that the elastic moduli measured in this study (ranging from 0.6 to 1.5 MPa) are lower than those of the Ti64 products (20–120 GPa) in published literature[61,62], which also exhibit higher relative density and minimal porosity. This discrepancy can be attributed to two primary factors. First, different porous metal AM methods yield different microstructures. For instance, Xiao et al.[63] printed the porous Ti64 structures using selective laser melting, which transiently increased the temperature above 1650 °C to induce rapid melting rather than comparatively slow solid-state sintering of Ti64 powders, enhancing the inter-powder bonding at the microscale as well as the mechanical properties at the macroscale. Second, potential residues remaining after heat treatment may weaken the mechanical properties of the porous Ti64 structures. To explore the composition of these residues, X-ray diffractometer (XRD) analyses are performed on the pure Ti64 powders as well as the Ti64 slurry ink before and after multi-step heat treatment. As shown in Fig. 3G, the XRD spectrum for the pure Ti64 powders exhibits the characteristic α peaks at the 2θ values of 35.5° (110), 38.5° (102), 40.5° (101), and 53.5° (102)[64]. When bentonite and PEGDA are added to prepare the slurry ink, the XRD spectrum predominantly displays the same characteristic peaks without additional distinct peaks from bentonite and PEGDA. This absence can be attributed to the low concentration of bentonite (4% (w/v)) in comparison to Ti64 (50% (v/v)) and the amorphous nature of PEGDA[65]. After heat treatment of the slurry ink at 1500 °C for 2, 4, and 6 h, the XRD spectra reveal the emergence of three sharp characteristic peaks corresponding to titanium carbide (TiC) at the 2θ values of 36.8°, 42.8°, and 62.9°. This indicates that carbon atoms, which remain in the structure after heat treatment[66], react with Ti64 at temperatures above 1350 °C to form TiC[67]. A low-intensity peak at 2θ of 27.5° is observed, which corresponds to the titanium dioxide (TiO_2) rutile phase (110)[68], suggesting the oxidation of Ti64 powders at elevated temperatures. As the sintering time increases, the intensity of Ti64 peaks decreases while TiC peaks become more pronounced, reflecting the ongoing carbonization of Ti64 powders. These undesired residues (i.e., TiC and TiO_2) result in the reduced mechanical properties of the sintered porous Ti64 structures. To mitigate Ti64 oxidation and carbonization, an inert gas such as helium[69] or argon[70] can be used to rapidly expel oxygen while providing a protective atmosphere for Ti64 powder sintering[52]. Additionally, advanced techniques like plasma[71] and microwave[72] sintering offer effective methods to minimize the presence of carbon monoxide and other carbon-based gases that promote TiC formation[70].

Freeform fabrication of diverse 3D structures via DC-DIW

After evaluating the effects of printing parameters and microstructure formation, three representative 3D structures with complex architectures are printed to demonstrate the printing capability of the proposed DC-DIW approach. First, a bifurcated tube is designed with two overhanging sections possessing an inclined angle of 45° (Fig. 4A1). Using the proposed DC-DIW approach, this bifurcated tube can be directly printed in air with precise architectural details, as illustrated in Fig. 4A2 and Movie S1. The bifurcated tube presents an outstanding self-supporting capability to sustain its shape before UV crosslinking due to the accurate control of interlayer distance and filament diameter. Following UV exposure, the PEGDA component in the tube forms a networked microstructure, providing the necessary stiffness for the subsequent heat treatment (Fig. 4A3). Then, the multi-step heat treatment is conducted on the tube to produce the bifurcated structure (Fig. 4A4). The heat treatment process begins with the removal of PEGDA and bentonite. Specifically, the pyrolysis temperature of bentonite is 800 °C, which is approximately half of the melting point of Ti64 (1660 °C). Therefore, solid-state sintering of Ti64 powders accompanies the beginning steps of the heat treatment, sufficiently bonding Ti64 powders to retain the tube's shape and preventing the risk of collapse. The key dimensions, such as tube height, width, and inner diameter, are measured and compared to the designed values, as summarized in Table S3. The relative errors are 6.95%, 6.51%, and 9.00%, respectively, indicating the high printing accuracy. The functionality of the bifurcated tube is demonstrated by injecting colored water into each channel. Yellow (Fig. 4A5) and black (Fig. 4A6) drips are observed at the tube's exit as different colored water is alternatively perfused, which is recorded in Movie S2, validating the operational effectiveness of the printed structure.

An orbital implant is designed (Fig. 4B1) to explore the potential biomedical application of the proposed DC-DIW approach. The printing process is shown in Fig. 4B2 and recorded in Movie S3. The key dimensions of the as-fabricated implant are measured in Table S4 with low relative errors along different directions, including 2.40% in length, 3.28% in width, and 6.67% in thickness. To illustrate its application in repairing an orbital fracture, a human skull model is partially reconstructed using FDM. Due to the implant's high accuracy, it can be smoothly inserted into the skull to patch the fracture, as illustrated in Fig. 4B4 and Movie S4.

Finally, a knee implant is designed (Fig. 4C1) and fabricated using the DC-DIW approach (Fig. 4C2 and Movie S5). The knee implant has the key dimensions of 43.88 mm in length, 53.34 mm in width, and 14.22 mm in height. The fabrication of this implant aims to validate the capability of the proposed approach to produce large-scale biomedical structures. After sintering, the dimensions of the knee implant (Fig. 4C3) are measured as listed in Table S5. The relative errors in length, width, and height are 5.33, 1.63, and 4.64%, respectively. This accuracy allows the knee implant to align

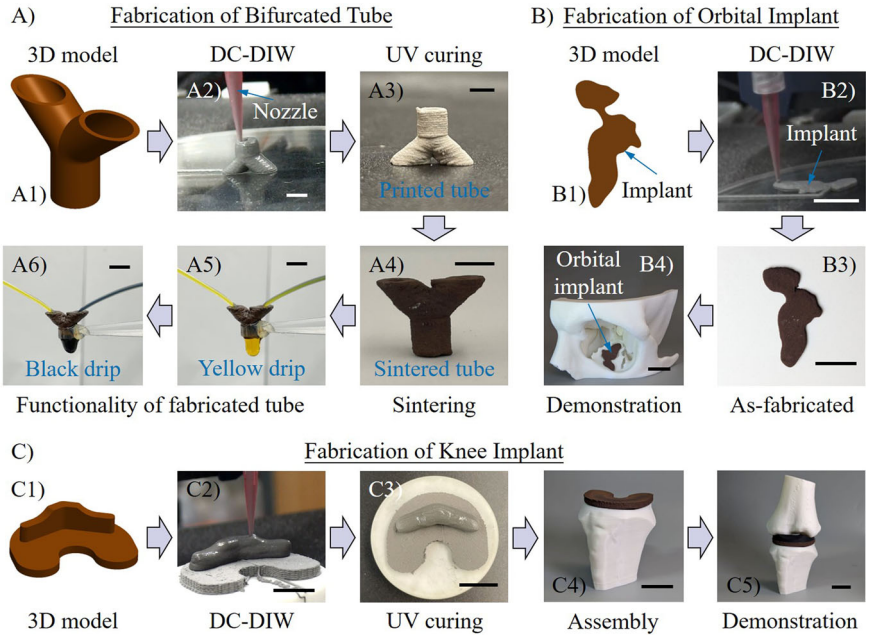

Fig. 4 | Representative structures printed by DC-DIW. A Fabrication of bifurcated tube: **A1** 3D model design, **A2** DC-DIW process, **A3** UV curing step, **A4** tube after heat treatment, and **A5** and **A6** dripping different colored water through the bifurcated tube. Scale bars: 10 mm. **B** Fabrication of orbital implant: **B1** implant design, **B2** DC-DIW of implant in air, **B3** implant after heat treatment, and **B4** implant aligned with the fractured skull. Scale bars: 15 mm. **C** Fabrication of knee implant: **C1** implant design, **C2** DC-DIW of implant, **C3** UV crosslinking of the implant, and implant assembling with **C4** tibia and **C5** femur. Scale bars: 20 mm.

precisely with a 3D-printed tibia (Fig. 4C4) to replace a knee damaged by arthritis. Additionally, the femur and synthetic meniscus are reconstructed using FDM and assembled with the tibia and knee implant, as shown in Fig. 4C5 and Movie S6. These results highlight the feasibility of using DC-DIW to fabricate customized biomedical components, demonstrating its reliability as an AM technique for diverse healthcare applications.

Discussion

Although Ti64 is selected as the exemplary titanium alloy in this work, the matrix ink proposed in the DC-DIW approach is miscible with other titanium alloys with enhanced biocompatibility for biomedical applications, e.g., titanium-6% aluminum-7% niobium and titanium-13% niobium-13% zirconium[73,74]. Additionally, other metals (such as tin, aluminum, zinc, and their alloys[75]) that have been printed by traditional DIW can also be produced and sintered through the DC-DIW approach. Moreover, ceramic oxides (e.g., alumina and zirconia[75,76]) and non-oxides ceramics (e.g., boron carbide and silicon nitride[75,76]) can be incorporated to prepare diverse slurry inks for the fabrication of end-use parts by DC-DIW. When printing these metallic and nonmetallic materials, three essential requirements must be fulfilled to design slurry inks. First, the effects of build material powder on the ink's rheology need to be considered. Generally, a yield stress (10–200 Pa) is needed to prepare self-supporting inks for DC-DIW, which enables slurry inks to maintain complex geometries and support subsequent layers[77]. In addition, a thixotropic recovery time below 1 s is typically required to ensure the rapid recovery of microstructures within slurry inks after extrusion through the nozzle[77]. Second, it is necessary to select a desired combination of sintering temperature and time which can guarantee the occurrence of solid-state sintering of powders when decomposing the bentonite powders. Finally, the powder size and concentration directly affect the porosity and average pore size of the printed parts after sintering and need to be carefully selected.

In this work, a "printing-then-solidification" strategy[36] is applied to print diverse 3D parts via DC-DIW. In this strategy, a liquid Ti64 structure is constructed in air and maintains its as-printed shape due to the self-supporting capability of the slurry ink. After printing, UV radiation is used to solidify the entire structure simultaneously. The advantage of this strategy is at the liquid state, adjacent layers can fuse well with each other to prevent the delamination defect. However, the use of "printing-then-solidification" limits the achievable maximum size. When a tall structure is printed, the maximum stress at the bottom layer may exceed the yield stress of the slurry ink, leading to the liquefication of the bottom layer and the collapse of the entire structure. To address this challenge, UV radiation can be integrated with DC-DIW to cause the gradual solidification of the bottom layer(s) as the current layer is being printed. Thus, it is technically feasible to print scaled-up 3D structures.

The mechanical performance and microstructures of titanium alloys differ significantly based on the applied AM methods. Usually, powder bed fusion techniques, like selective laser melting and electron beam melting, can produce titanium alloys with fully dense microstructures and enhanced elastic moduli (approximately 7.22 GPa)[78–80]. In contrast, DIW is featured by printing titanium parts with porous microstructures and relatively weak mechanical properties. For example, Coffigniez et al.[81] and Montufar et al.[79] produced titanium scaffolds with an average micropore size ranging from 15 to 20 μm and an average porosity of 13% through DIW and sintering, which are close to the pore size and porosity in this work. Specifically, Montufar et al.[79] performed the plasma sintering in the post-treatments and achieved scaffolds with an elastic modulus of 1.14 GPa. While a porosity range of 27–58%[82,83], an average pore size range of 300–600 μm, and an elastic modulus range of 2–19 GPa[82–84] are considered beneficial for cell proliferation of titanium bone implants, titanium implants with micropores below 20 μm, like those produced through DC-DIW, are necessary for applications that require increased surface area for cell attachment, greater absorption of bone inducing proteins, increased calcium and phosphate ion exchange, and the formation of apatite[81,85]. In addition, low porosities (5–10%) are beneficial for replicating the porosity of cortical bone and reducing the risk of fatigue failures[86,87]. Also, the reduced mechanical properties of titanium structures produced through DIW are efficient in preventing the stress-shielding effect and possible bone resorption at implant-bone interfaces[79]. Therefore, the proposed DC-DIW approach is more suitable for printing porous titanium products, like cortical and trabecular bone implants, for biomedical applications. To keep improving the mechanical properties of Ti64 parts in this work, three research directions can be delved into. First, the sintering temperature and time need to be further optimized based on the prediction of the developed PF modeling platform. Second, some advanced sintering techniques, such as spark plasma sintering[74] and microwave sintering[88], can be applied, which are promising to reduce the sintering time to less than 20 min while offering greater porosity control[51,89]. Finally, residuals in the heat treatment must be analyzed by some characterization techniques (like scanning electron microscope and

XRD) and well controlled through the use of inert gas and/or the application of these advanced sintering techniques.

In summary, a DC-DIW approach is developed to fabricate porous metals with intricate 3D structures. This approach employs a constant interlayer distance control method to ensure adequate contact area, overcoming the inclined angle limitation of current DIW techniques for printing overhanging architectures. By precisely controlling the interlayer distance and filament diameter, it is feasible to print overhanging features with an inclined angle of 30° without building external supporting scaffolds. A multi-step heat treatment is applied to regulate the microstructure by adjusting the sintering temperature and duration. Additionally, a phase-field modeling platform is established to theoretically predict the pore size and neck width of the as-fabricated parts. XRD analysis is conducted to identify undesired residues from the heat treatment, which weaken the mechanical properties. Lastly, the printed porous Ti64 structures, including the bifurcated tube, orbital implant, and knee implant, demonstrate the potential of the proposed DC-DIW approach for diverse future applications.

Because of the relatively weak mechanical performance of the as-fabricated parts, future work will focus on optimizing the multi-step heat treatment to prevent undesired carbonization and oxidation of Ti64 powders, aiming to propel the key mechanical properties to the end-user product level. In addition, comprehensive degradation studies will be conducted to evaluate the long-term stability and safety of the printed porous Ti64 implants under physiological conditions since one of the major applications of titanium alloys is to produce biomedical implants. For the theoretical studies, a 3D PF modeling platform will be established to more accurately predict the neck and pore evolution. Particularly, gas dynamics will be considered in the 3D simulation to understand the effects of gas expansion on solid-state sintering at specific temperatures and time durations. Finally, more biological studies, such as cytotoxicity, cell adhesion, proliferation, and differentiation, will be performed, which not only validate the functionality of the printed Ti64 for potential biomedical applications but also offer biological data to guide the design of the microstructure within the fabricated porous metals.

Methods

Ti64 slurry ink preparation

Ti64 was selected as the main metallic component to print the porous metal structures. The slurry ink was prepared following an identical protocol to that described in an earlier publication[30]. First, the matrix ink was prepared by diluting the stock polyethylene glycol diacrylate (PEGDA) solution (Mn 700, Sigma-Aldrich, St. Louis, MO) with deionized (DI) water to a concentration of 30% (v/v). Next, the photoinitiator (2-hydroxy-4'-(2-hydroxyethoxy)-2-methylpropiophenone, Sigma-Aldrich, St. Louis, MO) was dissolved in the diluted PEGDA at a concentration of 2% (w/v). Afterward, bentonite particles (Bentonite® clay, BYK Additives Inc., Gonzales, TX) were added to the solution at a concentration of 4% (w/v) and mixed uniformly using a glass rod. Finally, Ti64 powders (Ti-6Al-4V grade 5, AP&C, Boisbriand, Canada) were manually mixed into the matrix ink at a concentration of 50% (v/v) and then loaded into a syringe barrel for printing.

Customized DIW system and printing experiments

A customized DIW system was employed to print different structures from the Ti64 slurry ink. This system was based on a modified commercial FDM 3D printer (Kobra 2 Neo, Anycubic, Guangdong, China). The modification included the integration of a pneumatic control system (UltimusPlus I, EFD Nordson, Westlake, OH) to regulate the on/off status and dispensing pressure. A 20-gauge tapered nozzle with an inner diameter of 0.60 mm and length of 31.75 mm (EFD Nordson, Westlake, OH) was employed to print tubes with varying inclined angles (i.e., 30, 45, and 60°). The dispensing pressure was set at 0.3 bar (1 bar = 100 kPa) and the path speed was controlled at 7 mm/s. The standoff distance for the first layer was set at 0.75 mm. Three interlayer distances (i.e., 0.30, 0.45, and 0.60 mm) were tested to evaluate their effects on printing quality. The tube had a designed diameter of 20 mm and was made from a single filament per layer.

The same dispensing nozzle, pressure, and path speed were used to print various 3D structures from the Ti64 slurry ink. Specifically, a bifurcated tube with an overall height of 9.5 mm, an inclined angle of 45° at the bifurcation, and a diameter of 2.0 mm was designed using SolidWorks 2023 (Dassault Systems SolidWorks Corp., Waltham, MA) and sliced using the Cura 5.3.1 software (Ultimaker, Zaltbommel, Netherlands). The interlayer distance for this model was set at 0.45 mm. Additionally, the orbital and knee implant models were designed in SolidWorks 2023 and scaled to the appropriate sizes for demonstration, with interlayer distances set at 0.45 mm. A digital camera (DC-FZ80, Panasonic, Osaka, Japan) was utilized to document the printing processes and capture images of the printed structures.

UV curing and heat treatments

After printing, the structures were subjected to an ultraviolet (UV) curing system (OmniCure Series 2000, wavelength: 320–500 nm, Lumen Dynamics, Mississauga, Canada) to chemically crosslink the PEGDA component in the bifurcated tube, orbital implant, and knee implant. The UV light was positioned 10 cm from the printed structures, and the curing time was set at 60 min based on the previous work[30].

After UV crosslinking, the structures were transferred to a single-zone vacuum tube furnace (1700 °C 1-zone, Across International, Livingston, NJ) equipped with an alumina tube (Φ60 mm × 1000 mm in size, CT-60-100, Across International, Livingston, NJ) for the multi-step heat treatment. In the first and second steps, the furnace temperature was set at 500 and 800 °C, respectively, with a time duration of 2 h for each step. In the last step, three sintering temperatures (i.e., 1200, 1350, and 1500 °C) were tested to examine their effects on the formation of porous structures. All steps used a heating rate of 10 °C/min. The sintering time was varied at 2, 4, and 6 h to evaluate its impact. After sintering, the structures were cooled to room temperature within the furnace at a cooling rate of 10 °C/min before being removed from the furnace.

Mechanical property testing

The Ti64 slurry ink was perfused into a homemade, cylindrical polydimethylsiloxane (PDMS) mold to prepare the compression specimens (Φ12 mm × 5 mm). To crosslink the specimens, the mold was placed under the UV curing system for 60 min. After curing, the specimens were removed from the mold and transferred to the furnace for the multi-step heat treatment. Different sintering temperatures and durations were applied to study their effects on mechanical properties. After heat treatment, the specimens were subjected to uniaxial compression tests at room temperature using a mechanical tester (Model 3369, Instron Universal Testing Machine, Instron, MA). The compression speed was set at 0.5 mm/min. The force-displacement curves were recorded for each specimen, from which the stress-strain curves were derived. The elastic modulus of each specimen was then calculated from its respective stress-strain curves.

Microstructure characterization

The microstructures of the compression specimens were also characterized. The specimens sintered under different conditions were examined using a high-precision measurement system (Vertex 261, Micro-Vu, Windsor, CA) to assess the surface quality. The system was set to a magnification of 209× to image and measure the mesoscale pore size and the inter-particle neck width. After capturing the images, ImageJ software (https://imagej.nih.gov/ij/) was utilized for data processing. The enhanced function was applied to improve the contrast and visibility of the features of interest. Subsequently, the images were converted to 8-bit grayscale to standardize the data for analysis. A thresholding function was then employed to delineate the Ti64 particles from the surrounding pores, allowing for clear differentiation between solid and void regions. After compression, the sample remains were transferred into the sample cells and immersed in liquid nitrogen for further analysis. A Brunauer-Emmett-Teller (BET) specific surface area and pore size analyzer (Belsorp MINI X, Microtrac, York, PA) was used to measure

the nanoscale pore size of the specimens. Additionally, a helium gas pycnometer (BELPYCNO L, Microtrac, York, PA) was employed to determine the density of the specimens.

Phase-field modeling

To investigate solid-state sintering in this study, a qualitative two-dimensional phase-field (PF) model was employed using the Multiphysics Object-Oriented Simulation Environment (MOOSE), which was developed by the Idaho National Lab[55]. This model serves as a powerful tool for capturing microstructure evolution by minimizing the system's total free energy. The details on the application of PF modeling in various processes have been introduced in the previous studies[56,57] and summarized in the supporting information. The key material parameters utilized for simulating the sintering process of Ti64 powders were available in the literature[57–59].

Crystal structure analysis

To analyze the chemical composition and crystal structure of the Ti64 slurry ink during the sintering process, five grams of each sample were prepared. The samples included untreated Ti64 powders, untreated Ti64 slurry ink, and Ti64 slurry ink sintered at 1500 °C for 2, 4, and 6 h. Each sample was manually milled to a homogeneous powder using a mortar and pestle. The elemental composition and crystal structure of the resulting powders were analyzed by an X-ray diffractometer (XRD; D8 Advance, Bruker, Billerica, MA) equipped with a Cu-Kα conventional sealed X-ray tube, a goniometer assembly, and a LYNXEYE XE-T detector. The X-ray source was operated at 40 kV and 40 mA. The XRD measurements were performed using a θ-2θ configuration over a range of 3° to 90°.

Demonstration of as-fabricated 3D structures

Before the demonstration, the key dimensions of the bifurcated tube, orbital implant, and knee implant were measured by the high-precision measurement system. For the bifurcated tube, two tubings (0.5 mm inner diameter PTFE tubing, PerkinElmer, Waltham, MA) were inserted into the bifurcated sections. These tubings were connected to two syringe pumps (Pump 11 Elite, Harvard Apparatus, Holliston, MA, and NE-300 Just Infusion Syringe Pump, New Era Pump Systems Inc., Farmingdale, NY). DI water, alternatively with yellow and black dyes (McCormick, Hunt Valley, MD), was pumped into the bifurcated tube to simulate the process of switching fluids. The skull and leg bone models were printed on an FDM 3D printer (Super Racer, Flsun, Henan, China) using polylactic acid (PLA) fibers (1.75 mm, HATCHBOX, Los Angeles, CA). The printed implants were assembled with their respective models to demonstrate their clinical applications.

Statistical analysis

Except for the XRD, all the other quantitative values in the text and figures were reported as means ± standard deviation (SD) with n ($n = 3$) samples per group.

Data availability

All study data are included in the article and/or supporting information. Additional data are available from the corresponding author (yifeij@unr.edu) upon reasonable request.

Received: 30 September 2024; Accepted: 4 January 2025;
Published online: 04 February 2025

References

1. Nakajima, H. Fabrication, properties and application of porous metals with directional pores. *Prog. Mater. Sci.* **52**, 1091–1173 (2007).
2. Gao, J.-Y., Chen, S., Liu, T.-Y., Ye, J. & Liu, J. Additive manufacture of low melting point metal porous materials: capabilities, potential applications and challenges. *Mater. Today* **49**, 201–230 (2021).
3. Kränzlin, N. & Niederberger, M. Controlled fabrication of porous metals from the nanometer to the macroscopic scale. *Mater. Horiz.* **2**, 359–377 (2015).
4. Zhu, B. et al. Short review on porous metal membranes—fabrication, commercial products, and applications. *Membranes* **8**, 83 (2018).
5. Atwater, M. A., Guevara, L. N., Darling, K. A. & Tschopp, M. A. Solid state porous metal production: a review of the capabilities, characteristics, and challenges. *Adv. Eng. Mater.* **20**, 1700766 (2018).
6. Ryan, G., Pandit, A. & Apatsidis, D. P. Fabrication methods of porous metals for use in orthopaedic applications. *Biomaterials* **27**, 2651–2670 (2006).
7. Santos, G. The importance of metallic materials as biomaterials. *Adv. Tissue Eng. Regen. Med. Open Access* **3**, 300–302 (2017).
8. Veiga, C., Davim, J. P. & Loureiro, A. Properties and applications of titanium alloys: a brief review. *Rev. Adv. Mater. Sci.* **32**, 133–148 (2012).
9. Okazaki, Y., Ito, Y., Kyo, K. & Tateishi, T. Corrosion resistance and corrosion fatigue strength of new titanium alloys for medical implants without V and Al. *Mater. Sci. Eng. A* **213**, 138–147 (1996).
10. Manoj, A., Kasar, A. K. & Menezes, P. L. Tribocorrosion of porous titanium used in biomedical applications. *J. Bio- Tribo-Corros.* **5**, 3 (2018).
11. Wauthle, R. et al. Revival of pure titanium for dynamically loaded porous implants using additive manufacturing. *Mater. Sci. Eng. C* **54**, 94–100 (2015).
12. Jung, H.-D. Titanium and its alloys for biomedical applications. *Metals* **11**, 1945 (2021).
13. Pałka, K. & Pokrowiecki, R. Porous titanium implants: a review. *Adv. Eng. Mater.* **20**, 1700648 (2018).
14. Lee, H. et al. Customizable design of multiple-biomolecule delivery platform for enhanced osteogenic responses via 'tailored assembly system'. *Bio-Des. Manuf.* **5**, 451–464 (2022).
15. Lee, H. et al. Functionally assembled metal platform as lego-like module system for enhanced mechanical tunability and biomolecules delivery. *Mater. Des.* **207**, 109840 (2021).
16. Zhang, B. et al. The biomimetic design and 3D printing of customized mechanical properties porous Ti6Al4V scaffold for load-bearing bone reconstruction. *Mater. Des.* **152**, 30–39 (2018).
17. Kasar, A. K., Jose, S. A., D'Souza, B. & Menezes, P. L. Fabrication and tribological performance of self-lubricating porous materials and composites: a review. *Materials* **17**, 3448 (2024).
18. Yang, X.-L., Du, X.-F., Xu, Z.-L., Liang, Z.-S. & Xiong, L.-L. Progress in processing of porous titanium: a review. *Rare Metals* **43**, 1932–1955 (2024).
19. Singh, R., Lee, P. D., Dashwood, R. J. & Lindley, T. C. Titanium foams for biomedical applications: a review. *Mater. Technol.* **25**, 127–136 (2010).
20. Novák, P. Advanced powder metallurgy technologies. *Materials* **13**, 1742 (2020).
21. Hosford, W. F. & Duncan, J. L. Sheet metal forming: a review. *JOM* **51**, 39–44 (1999).
22. Wong, K. V. & Hernandez, A. A review of additive manufacturing. *Int. Sch. Res. Not.* **2012**, 208760 (2012).
23. Shishkovsky, I. V., Volova, L. T., Kuznetsov, M. V., Morozov, Y. G. & Parkin, I. P. Porous biocompatible implants and tissue scaffolds synthesized by selective laser sintering from Ti and NiTi. *J. Mater. Chem.* **18**, 1309–1317 (2008).
24. Murr, L. E. et al. Microstructures and mechanical properties of electron beam-rapid manufactured Ti–6Al–4V biomedical prototypes compared to wrought Ti–6Al–4V. *Mater. Charact.* **60**, 96–105 (2009).
25. Shi, J. et al. Design and fabrication of graduated porous Ti-based alloy implants for biomedical applications. *J. Alloys Compd.* **728**, 1043–1048 (2017).
26. Tan, X. P., Tan, Y. J., Chow, C. S. L., Tor, S. B. & Yeong, W. Y. Metallic powder-bed based 3D printing of cellular scaffolds for orthopaedic implants: a state-of-the-art review on manufacturing, topological

design, mechanical properties and biocompatibility. *Mater. Sci. Eng. C* **76**, 1328–1343 (2017).
27. Song, Y., Ghafari, Y., Asefnejad, A. & Toghraie, D. An overview of selective laser sintering 3D printing technology for biomedical and sports device applications: processes, materials, and applications. *Opt. Laser Technol.* **171**, 110459 (2024).
28. Yuan, L., Ding, S. & Wen, C. Additive manufacturing technology for porous metal implant applications and triple minimal surface structures: a review. *Bioact. Mater.* **4**, 56–70 (2019).
29. Chen, M., Zhang, D., Hsu, Y.-C. & Dunand, D. C. Microstructure and properties of high-entropy-superalloy microlattices fabricated by direct ink writing. *Acta Mater.* **275**, 120055 (2024).
30. Valentin, N. et al. Direct ink writing to fabricate porous acetabular cups from titanium alloy. *Bio-Des. Manuf.* **6**, 121–135 (2023).
31. Xu, C., Yu, S., Wu, W., Liu, Q. & Ren, L. Direct ink writing of Fe bone implants with independently adjustable structural porosity and mechanical properties. *Addit. Manuf.* **51**, 102589 (2022).
32. Huang, X., Ye, C., Wu, S., Guo, K. & Mo, J. Sloping wall structure support generation for fused deposition modeling. *Int. J. Adv. Manuf. Technol.* **42**, 1074–1081 (2009).
33. Xu, C., Quinn, B., Lebel, L. L., Therriault, D. & L'Espérance, G. Multi-material direct ink writing (DIW) for complex 3D metallic structures with removable supports. *ACS Appl. Mater. Interfaces* **11**, 8499–8506 (2019).
34. Jin, Y., Chai, W. & Huang, Y. Printability study of hydrogel solution extrusion in nanoclay yield-stress bath during printing-then-gelation biofabrication. *Mater. Sci. Eng. C* **80**, 313–325 (2017).
35. Jin, Y., Liu, C., Chai, W., Compaan, A. & Huang, Y. Self-supporting nanoclay as internal scaffold material for direct printing of soft hydrogel composite structures in air. *ACS Appl. Mater. Interfaces* **9**, 17456–17465 (2017).
36. Jin, Y., Compaan, A., Chai, W. & Huang, Y. Functional nanoclay suspension for printing-then-solidification of liquid materials. *ACS Appl. Mater. Interfaces* **9**, 20057–20066 (2017).
37. Frenkel, D., Ginsbury, E. & Sharabi, M. The mechanics of bioinspired stiff-to-compliant multi-material 3D-printed interfaces. *Biomimetics* **7**, 170 (2022).
38. Zhang, Y. et al. Carbazole-fused coumarin based oxime esters (OXEs): efficient photoinitiators for sunlight driven free radical photopolymerization. *Green Chem.* **25**, 6881–6891 (2023).
39. Monroe, B. M. & Weed, G. C. Photoinitiators for free-radical-initiated photoimaging systems. *Chem. Rev.* **93**, 435–448 (1993).
40. Ribas-Massonis, A., Cicujano, M., Duran, J., Besalú, E. & Poater, A. Free-radical photopolymerization for curing products for refinish coatings market. *Polymers* **14**, 2856 (2022).
41. Taheri, P., Maleh, M. S. & Raisi, A. Cross-linking of poly (ether-block-amide) by poly (ethylene glycol) diacrylate to prepare plasticizing-resistant CO_2-selective membranes. *J. Environ. Chem. Eng.* **9**, 105877 (2021).
42. Echalier, C., Valot, L., Martinez, J., Mehdi, A. & Subra, G. Chemical cross-linking methods for cell encapsulation in hydrogels. *Mater. Today Commun.* **20**, 100536 (2019).
43. Kalakkunnath, S., Kalika, D. S., Lin, H. & Freeman, B. D. Viscoelastic characteristics of UV polymerized poly(ethylene glycol) diacrylate networks with varying extents of crosslinking. *J. Polym. Sci. B Polym. Phys.* **44**, 2058–2070 (2006).
44. Zhang, Y., Yin, M.-J., Ouyang, X., Zhang, A. P. & Tam, H.-Y. 3D μ-printing of polytetrafluoroethylene microstructures: a route to superhydrophobic surfaces and devices. *Appl. Mater. Today* **19**, 100580 (2020).
45. Ramos Filho, F. G., Mélo, T. J. A., Rabello, M. S. & Silva, S. M. L. Thermal stability of nanocomposites based on polypropylene and bentonite. *Polym. Degrad. Stab.* **89**, 383–392 (2005).
46. Wang, J. et al. Energy absorption characteristics and preparation of porous titanium with high porosity. *Mater. Today Commun.* **34**, 105003 (2023).
47. Dabrowski, B., Swieszkowski, W., Godlinski, D. & Kurzydlowski, K. J. Highly porous titanium scaffolds for orthopaedic applications. *J. Biomed. Mater. Res. B Appl. Biomater.* **95B**, 53–61 (2010).
48. Rivard, J., Brailovski, V., Dubinskiy, S. & Prokoshkin, S. Fabrication, morphology and mechanical properties of Ti and metastable Ti-based alloy foams for biomedical applications. *Mater. Sci. Eng. C* **45**, 421–433 (2014).
49. Ozaydin-Ince, G. & Gleason, K. K. Thermal stability of acrylic/methacrylic sacrificial copolymers fabricated by initiated chemical vapor deposition. *J. Electrochem. Soc.* **157**, D41 (2009).
50. Jazi, H. R. S., Coyle, T. W. & Mostaghimi, J. Understanding grain growth and pore elimination in vacuum-plasma-sprayed titanium alloy. *Metall. Mater. Trans. A* **38**, 476–484 (2007).
51. Ogunmefun, O. A., Bayode, B. L., Jamiru, T. & Olubambi, P. A critical review of dispersion strengthened titanium alloy fabricated through spark plasma sintering techniques. *J. Alloys Compd.* **960**, 170407 (2023).
52. German, R. M. Titanium sintering science: a review of atomic events during densification. *Int. J. Refract. Met. Hard Mater.* **89**, 105214 (2020).
53. Yamanoglu, R., Bahador, A. & Kondoh, K. Fabrication methods of porous titanium implants by powder metallurgy. *Trans. Indian Inst. Met.* **74**, 2555–2567 (2021).
54. Basalah, A., Shanjani, Y., Esmaeili, S. & Toyserkani, E. Characterizations of additive manufactured porous titanium implants. *J. Biomed. Mater. Res. B Appl. Biomater.* **100B**, 1970–1979 (2012).
55. Tonks, M. R., Gaston, D., Millett, P. C., Andrs, D. & Talbot, P. An object-oriented finite element framework for multiphysics phase field simulations. *Comput. Mater. Sci.* **51**, 20–29 (2012).
56. Moelans, N., Blanpain, B. & Wollants, P. An introduction to phase-field modeling of microstructure evolution. *Calphad* **32**, 268–294 (2008).
57. Zhang, X. & Liao, Y. A phase-field model for solid-state selective laser sintering of metallic materials. *Powder Technol.* **339**, 677–685 (2018).
58. Yan, W., Ma, W. & Shen, Y. Powder sintering mechanisms during the pre-heating procedure of electron beam additive manufacturing. *Mater. Today Commun.* **25**, 101579 (2020).
59. Rizza, G., Galati, M. & Iuliano, L. A phase-field study of neck growth in electron beam powder bed fusion (EB-PBF) process of Ti6Al4V powders under different processing conditions. *Int. J. Adv. Manuf. Technol.* **123**, 855–873 (2022).
60. Yu, C., Cao, P. & Jones, M. I. Titanium powder sintering in a graphite furnace and mechanical properties of sintered parts. *Metals* **7**, 67 (2017).
61. Benedetti, M., Cazzolli, M., Fontanari, V. & Leoni, M. Fatigue limit of Ti6Al4V alloy produced by selective laser sintering. *Procedia Struct. Integr.* **2**, 3158–3167 (2016).
62. Suresh, S. et al. Mechanical properties and in vitro cytocompatibility of dense and porous Ti–6Al–4V ELI manufactured by selective laser melting technology for biomedical applications. *J. Mech. Behav. Biomed. Mater.* **123**, 104712 (2021).
63. Xiao, Z. et al. Study of residual stress in selective laser melting of Ti6Al4V. *Mater. Des.* **193**, 108846 (2020).
64. Lan, L. et al. Effects of laser shock peening on microstructure and properties of Ti–6Al–4V titanium alloy fabricated via selective laser melting. *Materials* **13**, 3261 (2020).
65. Chen, K. et al. Preparation and performances of form-stable polyethylene glycol/methylcellulose composite phase change materials. *J. Polym. Res.* **27**, 199 (2020).
66. Malo de Molina, P., Lad, S. & Helgeson, M. E. Heterogeneity and its influence on the properties of difunctional poly(ethylene glycol) hydrogels: structure and mechanics. *Macromolecules* **48**, 5402–5411 (2015).
67. Hu, C., Liu, J., Xu, L., Yu, L. & Zhu, B. Effect of sintering temperature on properties of carbon fiber-reinforced titanium matrix composites. *ACS Omega* **7**, 30087–30092 (2022).
68. Wang, M. et al. Fabrication and characterization of selective laser melting printed Ti–6Al–4V alloys subjected to heat treatment for customized implants design. *Prog. Nat. Sci. Mater. Int.* **26**, 671–677 (2016).

69. Amano, H. et al. Effect of a helium gas atmosphere on the mechanical properties of Ti-6Al-4V alloy built with laser powder bed fusion: a comparative study with argon gas. *Addit. Manuf.* **48**, 102444 (2021).
70. Peng, Q. et al. Fabrication of boronized Ti6Al4V/HA composites by microwave sintering in mixed gases. *ACS Omega* **5**, 11629–11636 (2020).
71. Hu, Z.-Y. et al. A review of multi-physical fields induced phenomena and effects in spark plasma sintering: fundamentals and applications. *Mater. Des.* **191**, 108662 (2020).
72. Batienkov, R. V., Bol'shakova, A. N. & Khudnev, A. A. Microwave sintering of metal powder materials (review). *Metallurgist* **65**, 1163–1173 (2022).
73. Fellah, M. et al. Tribological behavior of Ti-6Al-4V and Ti-6Al-7Nb alloys for total hip prosthesis. *Adv. Tribol.* **2014**, 451387 (2014).
74. Kong, Q. et al. Characterization and corrosion behaviour of Ti-13Nb-13Zr alloy prepared by mechanical alloying and spark plasma sintering. *Mater. Today Commun.* **23**, 101130 (2020).
75. Saadi, M. A. S. R. et al. Direct ink writing: a 3D printing technology for diverse materials. *Adv. Mater.* **34**, 2108855 (2022).
76. Shahzad, A. & Lazoglu, I. Direct ink writing (DIW) of structural and functional ceramics: recent achievements and future challenges. *Compos. B Eng.* **225**, 109249 (2021).
77. Mitchell, K., Hua, W., Bandala, E., Gaharwar, A. K. & Jin, Y. Particle–polymer interactions for 3D printing material design. *Chem. Phys. Rev.* **5**, 011304 (2024).
78. Mandal, S. et al. Study of pore morphology, microstructure, and cell adhesion behaviour in porous Ti-6Al-4V scaffolds. *Emergent Mater.* **2**, 453–462 (2019).
79. Montufar, E. B. et al. Benchmarking of additive manufacturing technologies for commercially-pure-titanium bone-tissue-engineering scaffolds: processing-microstructure-property relationship. *Addit. Manuf.* **36**, 101516 (2020).
80. Zhang, T. et al. Microstructure and biocompatibility of porous-Ta/Ti-6Al-4 V component produced by laser powder bed fusion for orthopedic implants. *Mater. Charact.* **182**, 111554 (2021).
81. Coffigniez, M. et al. Direct-ink writing of strong and biocompatible titanium scaffolds with bimodal interconnected porosity. *Addit. Manuf.* **39**, 101859 (2021).
82. Chen, Y. et al. Mechanical properties and biocompatibility of porous titanium scaffolds for bone tissue engineering. *J. Mech. Behav. Biomed. Mater.* **75**, 169–174 (2017).
83. Torres-Sanchez, C. et al. The effect of pore size and porosity on mechanical properties and biological response of porous titanium scaffolds. *Mater. Sci. Eng. C* **77**, 219–228 (2017).
84. He, S. et al. Effect of 3D-printed porous titanium alloy pore structure on bone regeneration: a review. *Coatings* **14**, 253 (2024).
85. Rodriguez-Contreras, A. et al. Powder metallurgy with space holder for porous titanium implants: a review. *J. Mater. Sci. Technol.* **76**, 129–149 (2021).
86. Xiong, Y. et al. Fatigue behavior and osseointegration of porous Ti-6Al-4V scaffolds with dense core for dental application. *Mater. Des.* **195**, 108994 (2020).
87. Zumofen, L. et al. Properties of additive-manufactured open porous titanium structures for patient-specific load-bearing implants. *Front. Mech. Eng*. **7**, 830126 (2022).
88. Balasundar, P., Senthil, S., Narayanasamy, P. & Ramkumar, T. Microstructure and tribological properties of microwave-sintered Ti0.8Ni–0.3Mo/TiB composites. *Ceram. Int.* **49**, 6055–6062 (2023).
89. Tang, C. Y. et al. In situ formation of Ti alloy/TiC porous composites by rapid microwave sintering of Ti6Al4V/MWCNTs powder. *J. Alloys Compd.* **557**, 67–72 (2013).

Acknowledgements

L.R. acknowledges the support of the National Science Foundation (NSF) Graduate Research Fellowship Program (AWD0002282-1937966). Y.J. and X.W. acknowledge the support of the Nevada NASA Space Grant Consortium (80NSSC20M0043). The X-ray diffractometer was purchased with NSF support (CHE-1429768).

Author contributions

E.B.: Writing—review & editing, Writing—original draft, Visualization, Methodology, Investigation, Formal analysis, Data curation, Conceptualization. L.R.: Writing—original draft, Visualization, Methodology, Investigation, Formal analysis, Data curation. K.M.: Writing—original draft, Visualization, Methodology, Investigation, Formal analysis, Data curation. F.R.: Methodology, Investigation, Formal analysis, Data curation. J.T.: Methodology, Investigation, Formal analysis, Data curation. B.O.: Methodology, Investigation, Formal analysis, Data curation. A.K.: Methodology, Investigation, Formal analysis, Data curation. M.E.: Writing—review & editing, Supervision. J.S.: Writing—review & editing, Supervision. X.Z.: Methodology, Investigation, Formal analysis. P.M.: Writing—review & editing, Supervision. X.W.: Writing—review & editing, Supervision, Funding acquisition. P.C.: Writing—review & editing, Supervision. Y.L.: Writing—review & editing, Writing—original draft, Supervision, Project administration. Y.J.: Writing—review & editing, Writing—original draft, Supervision, Project administration, Funding acquisition, Conceptualization.

Competing interests

The authors declare no competing interests.

Additional information

Supplementary information The online version contains supplementary material available at https://doi.org/10.1038/s44334-025-00016-1.

Correspondence and requests for materials should be addressed to Pradeep L. Menezes, Xiaoliang Wang, Pengbo Chu, Yiliang Liao or Yifei Jin.